On the effects of a separation bubble on fan noise

Jean Al-Am, Vincent Clair, Alexis Giauque, Jérôme Boudet, Fernando Gea-Aguilera

On the effects of a separation bubble on fan noise

Jean Al-Am[a,1], Vincent Clair[a], Alexis Giauque[a], Jérôme Boudet[a], Fernando Gea-Aguilera[b]

[a] *Univ Lyon, École Centrale de Lyon, INSA Lyon, Université Claude Bernard Lyon I, CNRS, Laboratoire de Mécanique des Fluides et d'Acoustique, UMR 5509, 36 Avenue Guy de Collongue, F-69134, Ecully, France*
[b] *Safran Aircraft Engines, 77550 Moissy-Cramayel, France*

Abstract

A scale model of a fan stage operating at approach condition is investigated using wall-resolved Large Eddy Simulations. The configuration is a state-of-the-art fan stage (rotor + stator) of an Ultra High Bypass Ratio turbofan engine, and the computational cost has been reduced by simulating a radial slice of a periodic sector. At low fan speeds and Reynolds number, a recirculation bubble can be observed on the suction side of the fan blades, near the leading edge. This recirculation bubble causes the boundary layer transition to turbulence and is associated with high levels of wall pressure fluctuations. The noise spectra upstream of the fan blades show high frequency tones, which are related to the noise generation mechanism of the recirculation bubble. It has been found that the size, position and pressure disturbances in the bubble depend on the mass flow rate. Furthermore, the frequencies and amplitudes of the high frequency tones in the noise spectra also depend on the mass flow rate. As the mass flow rate decreases, the size of the bubble increases, the bubble shifts towards donwstream locations, and high levels of wall pressure fluctuations can be found along the suction side of the fan blade. The acoustic signature of the bubble shifts towards lower frequencies with the mass flow rate, but its amplitude increases. A coherence analysis and a Dynamic Mode Tracking technique are used to confirm that high frequency tones can be generated by the recirculation bubble in the separation region. The flow features at these frequencies suggest that a vortex shedding mechanism is related to the noise radiated from the recirculation bubble.

Keywords: Aeroacoustics, fan noise, broadband noise, recirculation bubble, large eddy simulations, direct noise computation

[1] PhD candidate, Ecole Centrale de Lyon, LMFA, jean.al-am@ec-lyon.fr.

Nomenclature

CD	Controlled-Diffusion
DMT	dynamic mode tracking
DNS	direct numerical simulations
LE	leading edge
LES	large eddy simulations
NSCBC	Navier-Stokes characteristic boundary conditions
OGV	outlet guide vanes
PSD	power spectral density
RANS	Reynolds-averaged Naviers-Stokes
RMS	root-mean-square
TE	trailing edge
TTGC	Two-step Taylor Galerkin Convection
WR	wall resolved
c	chord length, [m]
Re	Reynolds number
M	Mach number
α	angle of attack, [°]
B	fan blade count
V	stator vane count
Ω_n	nominal rotation speed, [RPM]
Ω	rotation speed, [RPM]
ω	angular speed, [rad/s]
BPF	blade passing frequency, [Hz]
VPF	vane passing frequency, [Hz]
HFP	high frequency peak, [Hz]
$\dot{m}$	mass flow rate, [kg/s]
p_{tot}	total pressure, [Pa]
$p_{\mathrm{tot},0}$	free-stream total pressure, [Pa]
p	static pressure, [Pa]
T_{tot}	total temperature, [K]
ρu	streamwise momentum, [kg m/s^2]
x, y, z	streamwise, transverse and spanwise directions, [m]
x^+, y^+, z^+	dimensionless wall distances
λ_{ac}	acoustic wavelength, [m]
λ_{Ta}	Taylor micro-scale, [m]
ν	kinematic viscosity, [m^2/s]
k_t	turbulent kinetic energy, [m^2/s^2]
ϵ	turbulent dissipation rate, [m^2/s^3]
f	frequency, [Hz]
f_c	cut-off frequency, [Hz]
P_{rms}	RMS pressure fluctuations, [Pa]
M_{is}	isentropic Mach number
γ	ration of specific heats

C_f	friction coefficient
δ_{TE}	boundary layer thickness at the trailing edge, [m]
δ_1	boundary layer displacement thickness, [m]
δ_2	boundary-layer momentum thickness, [m]
H_{12}	boundary-layer form factor, [m]
$\bar{u}$	moving average of a velocity component, [m/s]
u'_{rms}	moving average of RMS velocity fluctuations, [m/s]
u	streamwise velocity component, [m/s]
U	velocity magnitude, [m/s]
U_0	free-stream velocity magnitude, [m/s]
ρ_0	free-stream density, [kg/m^3]
ρ	density, [kg/m^3]
θ	angular angle, [°]
$\theta_{\max}$	angular sector of a single fan blade passage, [°].
b	wake half-width, [m]
x	streamwise direction [m]
m	azimuthal order
t	time, [s]
i	imaginary unit
γ^2	coherence
p_w	wall pressure fluctuations, [Pa]
p'	pressure fluctuations, [Pa]
St	Strouhal number
f_v	frequency of the vortex shedding, [Hz]

1. Introduction

One of the main contributors to the noise emitted by modern turbofan engines is the fan stage. The next generation of Ultra High Bypass Ratio (UHBR) engines is expected to improve the propulsive efficiency. To this end, the fan diameter will increase, whereas the jet exhaust speed will decrease. Furthermore, a short and thin nacelle will be used to reduce drag, such that the available space for acoustic liners could be reduced. Consequently, the contribution of the fan noise to the overall noise level is expected to be increased [1, 2].

The dominant fan noise sources are (i) the fan tip leakage flow noise, (ii) the turbulence interaction noise and (iii) the airfoil self-noise [3, 4]. The tip leakage flow noise is associated with the highly unsteady flow that develops in the gap between the tip of the fan blades and the outer casing. This highly unsteady flow can be diffracted at the Trailing Edge (TE) corner of the blade tip and interact with neighboring blades to generate noise. Turbulence interaction noise is produced as the turbulent wakes of the fan blades impinge on the Leading Edge (LE) of the Outlet Guide Vanes (OGV). The coherent and periodic component of the wakes, i.e. the wake velocity deficit, produces tonal

noise at the blade passing frequency, whereas the stochastic component of the wakes, i.e. the turbulent flow, produces broadband noise. The airfoil self-noise is associated with the turbulent flow that develops in the boundary layers of the fan blades and OGV. Self-noise has been shown to be a significant noise source in many applications, such as wind turbines [5], low speed ventilation fans [6] and aero-engines [7], and has been the motivation for several studies [8, 9, 10].

When the flow remains attached along the surface of an airfoil with a sharp TE, the turbulent eddies in the boundary layer are diffracted when passing the TE and generate noise. This is usually the case for a fan stage at its nominal operating regime. At low fan speeds, such as at approach conditions, a flow separation region may appear close to the LE of the fan blades, which may produce a recirculation bubble. This phenomenon and its contribution to the self-noise have been extensively studied experimentally [11, 12, 13, 14] and numerically [15, 16, 17, 18, 18, 19, 20] on a single airfoil configuration.

Direct Numerical Simulations (DNS) of the airflow around a NACA0012 airfoil were performed by Sandberg *et al.* [15, 16] at Reynolds and Mach numbers of $Re = 5 \times 10^4$ and $M = 0.4$, respectively. They assessed the capability of an analytical model, in which the airfoil is assimilated to a flat plate aligned with the flow, to predict self-noise from an airfoil at non-zero angle of attack ($\alpha \neq 0°$). Sandberg *et al.* [15, 16] observed that a laminar separation bubble can be found on the suction side of an airfoil at low Reynolds number flow and non-zero angle of attack. This separation bubble is followed by a transition to turbulence and a reattachment of the boundary layer. The noise results from the DNS indicate the presence of an additional noise source on the suction side that is not located at the TE and can change significantly the noise directivity. Similar conclusions found by Jones *et al.* [17], who observed that this additional noise source was dominant at high frequencies.

Another DNS study was performed by Wu *et al.* [18], who investigated the flow around a Controlled-Diffusion (CD) airfoil at $\alpha = 8°$, $Re = 1.5 \times 10^4$ and $M = 0.25$. Downstream of the LE, the flow is laminar and spanwise coherent structures are generated due to the Kelvin-Helmholtz instability [21, 22, 23]. This is related to a short recirculation bubble in the separation region that triggers the laminar to turbulent transition of the boundary layer. Downstream of the transition region, the size of the turbulent structures decreases as they are convected, and the turbulence is fully developed at the TE. Inside the separation region, a hump is observed in the amplitude of the wall pressure spectra. In this region, the space-time correlation of the fluctuating pressure shows a periodic pattern in time and significant levels of correlation in space due to large coherent spanwise structures. Similar results were obtained by Sanjosé *et al.* [24] using the Lattice-Boltzmann method with a DNS resolution for low Mach and Reynolds numbers and by Deuse *et al.* [19] and Shubham *et al.* [20] using Large Eddy Simulations (LES). The axial position of the separation region and the velocity fluctuations in this region are observed to significantly oscillate, generating additional noise.

Experimental studies using airfoils at low Mach and Reynolds numbers and high angles of attacks [13, 14] have shown an increase in the amplitude of the

velocity fluctuations in the separation region. This occurs close to the LE and is due to the onset of a recirculation bubble in the separation region. Experimental results from Kurelek *et al.* [14] exhibit evidence of a triple peak pattern for the profiles of the Root-Mean-Square (RMS) streamwise velocity fluctuations and a significant increase in the RMS velocity fluctuations normal to the airfoil surface. Additionally, Michelis *et al.* [13] show a dominant broadband peak in the Power Spectral Density (PSD) of the velocity fluctuations in the bubble region, which is related to Kelvin-Helmholtz instabilities.

Based on the observations discussed above, high angles of attack can be found at the fan LE at approach conditions, unlike those at cruise conditions. This might be related to the reduced freestream Mach number and fan rotational speed at approach conditions, which may result in local flow separations and in a recirculating bubble near the LE [10, 25, 26]. A recirculation bubble plays an important role in the boundary layer transition to turbulence on the fan blade surface and produces an additional noise source that can be associated with a highly unsteady flow in the bubble region [26]. It should be noted that a classical solution to suppress a laminar separation bubble consists of increasing the roughness (e.g. using a tripping band) near the LE in order to force the transition to turbulence before the flow separation [27, 28]. However, the use of a tripping band near the LE to prevent a separation bubble at approach conditions could increase aerodynamic losses at cruise conditions.

Although the presence of a recirculation bubble has been observed and was suggested as a significant noise contributor to the fan noise [26], a detailed analysis of the flow in the bubble and its acoustic signature in aero-engine applications have received limited attention. The objective of the present work is to improve current understanding of the unsteady aerodynamic characteristics and the noise generation mechanisms of a recirculation bubble in a state-of-the-art fan stage, by using LES. Particularly, this paper focuses on the effects of the mass flow rate, i.e. the angle of attack, on the evolution of the bubble and its acoustic signature.

This is achieved by performing a number of wall-resolved LES with varying mass flow rates. To reduce the computational cost, only a radial slice of a periodic angular sector of the fan-OGV stage is considered. Meshes were designed such that the acoustic propagation is resolved by the LES up to one chord length (c) upstream of the fan. The effects of the mass flow rate are analyzed in terms of the steady and unsteady characteristics of the flow in the vicinity of the fan blade surface, and the noise contributions that can be attributed to the recirculation bubble. To this end, a Dynamic Mode Tracking (DMT) method is used to examine the behavior of the flow at any frequency of interest for the recirculation bubble.

The paper is organized as follows. Section 2 presents a description of the computational domain, the characteristics of the meshes and the numerical parameters. The statistical and numerical convergence of the LES simulations, and a mesh convergence study are shown in Section 3. Finally, the effects of the mass flow rate on the formation of the recirculation bubble and its acoustic signature are presented in Section 4 for a reduced computational domain of a

state-of-the-art fan stage.

2. Large Eddy Simulation numerical setup

2.1. Computational domain and operating conditions

The geometry used for the present LES is the ECL5 fan/OGV stage [29, 30], which has been designed at École Centrale de Lyon. This state-of-the-art fan stage is composed of $B = 16$ rotor blades and a low-count stator with $V = 31$ vanes. In order to reduce the computational cost of the simulations, the original 16 blades and 31 vanes configuration has been adapted to 32 vanes to allow for a $2\pi/16$ angular periodicity. According to Rai *et al.* [31], the stage performance is kept constant by adjusting the vane chord length to maintain the same solidity, which is defined as the ratio between the chord length and the inter-vane spacing. For further computational cost reduction, only a radial slice (presented in Figure 1) representing 12% of the complete span (i.e. a span of 12 mm) is simulated. To assess whether the spanwise extent is large enough, the spanwise correlation length was calculated at a streamwise position in the recirculation bubble region. The spanwise extent was found to be approximately 3.5 times longer than the maximum turbulence length scale. This implies that the current spanwise computational domain size is suitable for a statistically independent acoustic source region and is considered to be valid for the present study.

RANS computations have been performed in order to compare the performance of the modified and original configurations. Both configurations show a similar flow topology and aerodynamic performances, which validates the modified vane count for the present study. The slice is centered at a radial position that corresponds to 80% of the hub-to-tip distance, and the blade and vane cross-section is kept constant in the spanwise direction. According to the full-span RANS results, the position of the radial layer at 80% minimizes 3D-effects and the radial velocity component.

An overview of the computational domain and the main geometrical dimensions are shown in Figure 1. The domain extends from 3.75 fan chord lengths upstream of the fan to 4.25 vane chord lengths downstream of the stator.

The nominal rotation speed of the ECL5 fan is $\Omega_n = 11000\,\mathrm{RPM}$. The LES are performed at approach conditions with a rotation speed of $\Omega = 0.55\Omega_n = 6050$ RPM, which leads to a circumferencial Mach number of 0.48 at the radial location of the slice, and a Blade Passing Frequency BPF = 1613 Hz. At the inlet section, the axial Mach number is set to 0.3 and the relative Mach number is set to 0.56. Thus, the fan operates in a fully subsonic regime. At approach conditions, the reference mass flow rate is $\dot{m} = 20\,\mathrm{kg/s}$ (full span), and the total pressure ratio is 1.1. The Reynolds number based on the chord length is approximately 10^6. Additionally, three other values, which correspond to full span flow rates of 19 kg/s, 21 kg/s and 22 kg/s, are considered in this study.

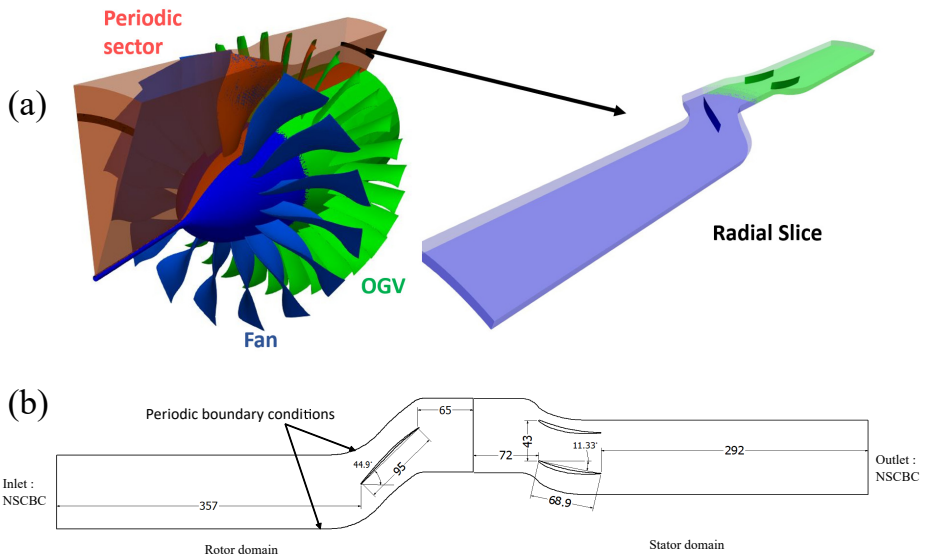

Figure 1: (a) Radial slice sector of the Fan/OGV stage. (b) Blade-to-blade view of the ECL5 fan/OGV configuration at 80% of the span. Dimensions are given in mm. Angles are given in degrees.

2.2. LES numerical parameters

The TurboAVBP solver is used to solve the LES governing equations in the present work. It is an explicit unstructured compressible LES code that has been developed at CERFACS [32]. For the present application, two LES domains are coupled. The first one is a rotating domain that contains the fan blade, and the second domain contains the 2 stator vanes. The data exchange between the two domains is performed by using the cwipi library developed by ONERA [33].

The filtered compressible Navier-Stokes equations are solved using a finite-volume Two-step Taylor Galerkin Convection (TTGC) scheme [34], which is a third-order convective numerical scheme in space and time. The unresolved turbulent eddies are modeled using the SIGMA subgrid-scale model [35]. At the inlet and outlet sections of the computational domain, non-reflecting Navier-Stokes characteristic boundary conditions (NSCBC) [36] are used. At the inlet section, the flow is purely axial and uniform without turbulence injection and total pressure and temperature are imposed (total pressure $p_{\text{tot}} = 101325\,\text{Pa}$ and total temperature $T_{\text{tot}} = 300\,\text{K}$). At the outlet section, the static pressure is adjusted to match the streamwise momentum ρu upstream of the rotor, as obtained from a full-span RANS simulation with the target mass flow rate. A periodic boundary condition is used on the circumferential sides of the computational domain, whereas a slip wall boundary condition is used at the boundaries in the radial direction. On the surface of the blades and vanes, a no-slip wall boundary condition is used. Two rotor rotations are required for the numerical

and statistical convergence (see Section 3), and four additional rotations for the acoustic data collection.

2.3. Mesh characteristics

Details of the LES grid are shown in Figure 2. The hybrid unstructured mesh is composed of prismatic cells on the blade walls, tetrahedral cells away from the blades, and pyramidal cells in the transition region between the prismatic and the tetrahedral cells. The mesh was designed based on turbulent and acoustic criteria established in a recent work of the authors [37]. In order to obtain a suitable spatial resolution to fully resolve the boundary layer on the airfoil surfaces, the mesh is particularly refined in this region. The first layer near the wall corresponds to the smallest spacing normal to the wall, and the cell size increases progressively away from the wall. Using prism layers on the walls, the values of x^+, y^+ and z^+ can be chosen in the appropriate ranges for wall-resolved LES. At reference mass flow rate, three different meshes have been designed and the properties of each mesh are presented in Table 2. These meshes differ by the number of prismatic layers and the growth ratio of the prisms. Away from the walls, mesh refinement is controlled by two main criteria:

- The number of points per acoustic wave-length $\lambda_{ac} = \frac{c_0(1-M)}{f_c}$, where c_0 is the speed of sound, M is a mean Mach number, and f_c is the desired mesh cut-off frequency.

- A constant "A" that is the ratio of the mesh size to the Taylor micro-scale $\lambda_{Ta} = (10\frac{\nu k_t}{\epsilon})^{(1/2)}$, where ν is the kinetic viscosity, k_t the turbulent kinetic energy, and ϵ the turbulent dissipation rate.

According to a previous study by the authors [37] using a similar mesh topology and numerical scheme, 13 points per λ_{ac} and a value $A = 30$ are adopted. The latter condition implies that the mesh size is limited to 30 times the Tylor micro-scale to reduce the computation expense while providing a good resolution for the turbulent structures. The main refinement regions of the mesh that follow the above criteria are listed below.

- Upstream of the rotor and downstream of the stator. The mesh is refined over one blade chord length upstream of the LE of the rotor and one vane chord length downstream of the TE of the stator in order to ensure a correct acoustic propagation in these regions up to 30 kHz.

- Rotor-stator interstage. The refinement of the mesh at the interstage ensures that the fan wakes are correctly propagated between the TE of the fan blades and the LE of the vanes.

- Around the blades. A smooth transition region between the prismatic layers and the tetrahedral cells has been ensured for all the meshes used in this study.

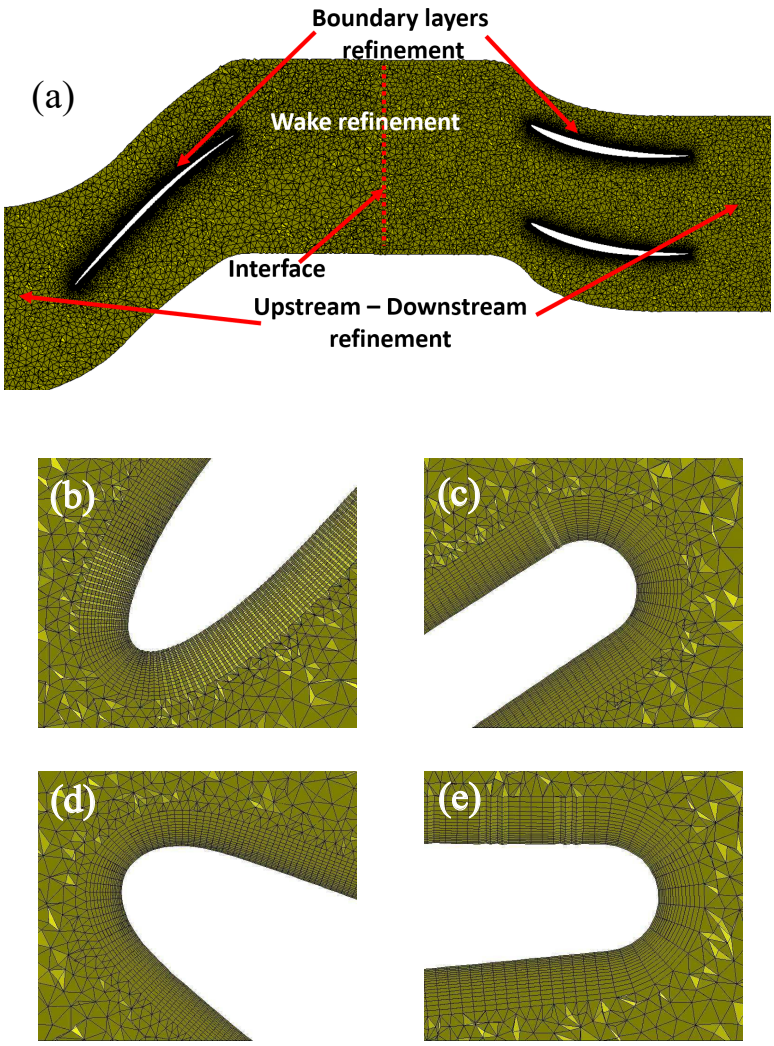

Figure 2: Blade-to-blade view of the mesh in the mid-span plane. (a) Rotor and stator domains (the mesh resolution is four times coarser than WRMesh1). (b) Rotor LE. (c) Rotor TE. (d) Stator LE. (e) Stator TE.

Table 2: Mesh properties for the different LES. x^+, y^+ and z^+ are the dimensionless wall distances in the streamwise, normal and spanwise directions, respectively.

	WR-Mesh1	WR-Mesh2	WR-Mesh3
Number of cells [10^6]	68	80	100
$x^+ = z^+$	35	35	35
y^+	1.0	1.0	1.0
Number of prismatic layers	8	16	24
Stretching ratio [%]	12	6	3
Time step [10^{-8}s]	0.8	0.8	0.8
CPUh/blade passage [10^3]	238	280	350

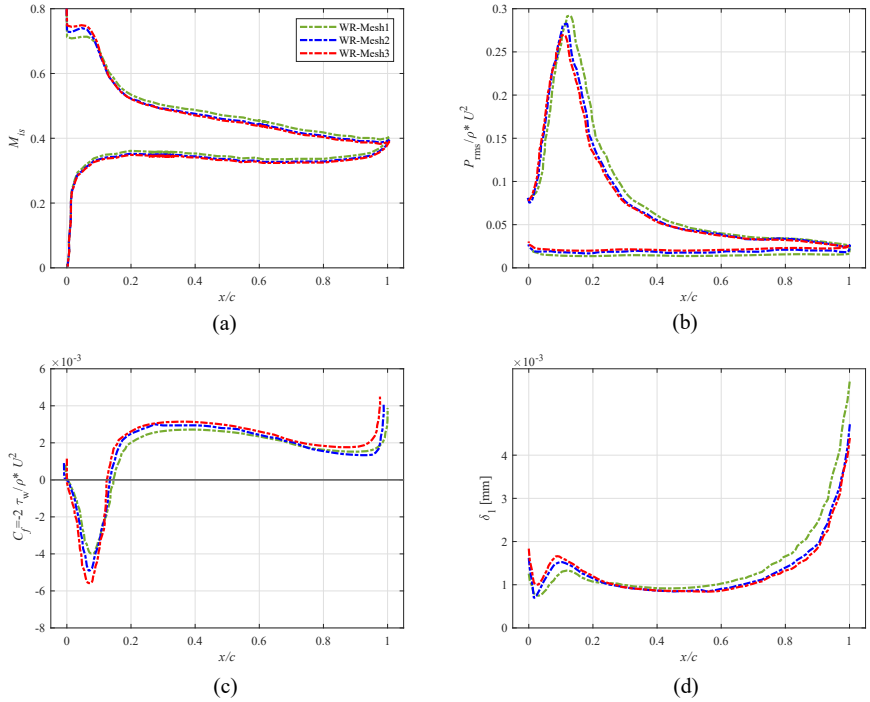

Figure 3: Mesh convergence. (a) The isentropic Mach number M_{is} and (b) RMS pressure fluctuations P_{rms} along the rotor blade. (c) The friction coefficient C_f and (d) boundary layer displacement thickness δ_1 along the suction side of the rotor blade. ρ is the density and τ_w is the wall shear stress.

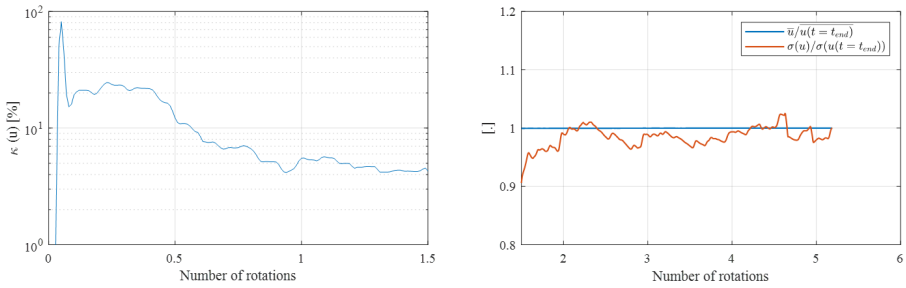

(a) (b)

Figure 4: Time convergence for the WR-Mesh2 case. (a) Numerical convergence. The number of rotations corresponds to the end of the first segment. (b) Statistical convergence. The mean value of ($\bar{u}$) and the standard deviation ($\sigma(u)$) of the streamwise velocity component are normalized by their values at the end of the simulation ($t = t_{end}$, where "t" corresponds to the time).

3. LES convergence criteria

3.1. Mesh convergence

In this section, the mesh convergence of the LES is assessed by comparing the results from the 3 meshes presented in Table 2, for the reference mass flow rate $\dot{m} = 20\,\mathrm{kg/s}$. Figure 3 shows comparison between the different meshes for several quantities characterizing the mean flow (isentropic Mach number, friction coefficient, boundary layer thickness) and the fluctuations (RMS pressure fluctuations P_{rms}) in the vicinity of the fan blade surface. The isentropic Mach number M_{is} is defined as,

$$M_{is} = \sqrt{\left(\left(\frac{p_{\mathrm{tot},0}}{p}\right)^{\frac{\gamma-1}{\gamma}} - 1\right)\frac{2}{\gamma-1}},$$

where $p_{\mathrm{tot},0}$ is the total pressure in the free-stream outside the boundary layers, p is the static pressure and γ is the ratio of specific heats (in this case $\gamma = 1.4$). The friction coefficient C_f and boundary layer displacement thickness δ_1 are shown for the suction side only, where the separation bubble appears. Overall, the results show a good agreement between the different meshes along the blade chord length. The distributions of M_{is} and P_{rms} on the pressure side are close for the 3 meshes. On the suction side, near the LE, a separation zone can be associated with a region of negative friction coefficient and a plateau of isentropic Mach number. It should be noted that high pressure fluctuations are also observed in that region. Some discrepancies between WR-Mesh1 and WR-Mesh3 results can be seen for all the quantities in Figure 3, particularly in the separation region. These differences are more pronounced for δ_1 over the whole suction side, where WR-Mesh1 predicts a faster increase of the thickness of the boundary layer. This may be due to differences in the laminar to turbulence

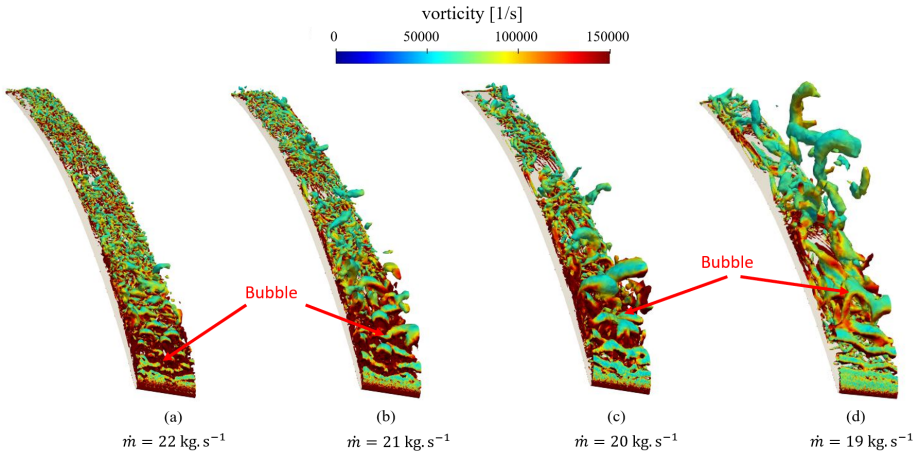

Figure 5: Iso-surfaces of Q-criterion ($Qc^2/U_0^2 = 1500$), colored by the vorticity magnitude, for the different mass flow rates. The cases are shown by decreasing mass flow rate, and increasing the angle of attack of the fan blade.

transition, which may lead to cumulative discrepancies. When comparing WR-Mesh2 and WR-Mesh3, similar results are obtained for the different quantities in Figure 3 along the whole blade surface. This justifies the use of WR-Mesh2 to study of the effects of the mass flow rate in Section 4.

3.2. Time convergence

Temporal convergence is necessary to ensure proper physical analysis. Two different types of temporal convergence are studied here for the mesh WR-Mesh2 at a mass flow rate of $\dot{m} = 20\,\mathrm{kg/s}$. The first type of convergence is referred to as numerical convergence and corresponds to the end of the transient state. The second type of convergence is referred to as statistical convergence and corresponds to the convergence of the flow statistics. Unsteady velocity samples were collected for the convergence analysis. These were obtained from the suction side boundary layer near the fan TE, at a normalized wall-normal distance of $y^+ = 50$. Based on the convergence analysis methodology introduced by Boudet *et al.* [38], the velocity signal is split into four segments and statistical estimates based on the last three segments are compared. The convergence is estimated by introducing the function

$$\kappa(u) = \max\left(\max_{i,j=2..4}\left(\left|\frac{\overline{u}^{(i)} - \overline{u}^{(j)}}{\overline{u}^{(4)}}\right|\right), \max_{i,j=2..4}\left(\left|\frac{u'^{(i)}_{RMS} - u'^{(j)}_{RMS}}{u'^{(4)}_{RMS}}\right|\right)\right) \times 100 \tag{1}$$

where $\overline{u}^{(i)}$ and $u'^{(i)}_{RMS}$ are the moving average of a velocity component and the moving average of RMS velocity fluctuations, respectively, which are calculated

Table 3: Fan blade angle of attack α for various mass flow rates $\dot{m}$.

$\dot{m}$ [kg/s]	19	20	21	22
α [°]	12.5	9.10	7.40	5.30

over the i-th segment. The evolution of $\kappa(u)$ is presented in Figure 4 (a). Numerical convergence is reached when κ stabilizes within a few per cent (4% in this case), which corresponds to the end of the first segment. The statistics are then calculated from this point.

The statistical convergence is considered to be reached when the statistics reach a constant value. Figure 4 (b) shows the evolution of the mean ($\overline{u}$) and the standard deviation ($\sigma(u)$) of the streamwise velocity component (u), both normalized by values at the end of the simulation. It can be observed that the simulation is well converged after 1.5 rotations.

4. Effects of the mass flow rate

In this section, the mesh WR-Mesh2, which has been shown to properly describe the separation bubble in Section 3, is adopted. The effects of the mass flow rate on the characteristics of the bubble and the generated noise are studied by comparing the results for four different mass flow rates ranging from 19 to 22 kg/s.

4.1. Aerodynamic results

The increase of the fan blade angle of attack α with the mass flow rate $\dot{m}$ (shown in Table 3) is expected to cause variations of the recirculation bubble characteristics, which are detailed in the following.

The turbulent structures on the suction surface of the rotor blade are shown in Figure 5, for the different mass flow rates, using iso-surfaces of the Q-criterion ($Qc^2/U_0^2 = 1500$, where U_0 is the free-stream velocity magnitude) colored by the vorticity magnitude. For all the cases, a laminar boundary layer is formed near the LE, followed by a transition region, where a recirculation bubble is identified. This bubble is characterized by a significant level of vorticity and forces the transition of the boundary layer to turbulence. Downstream of the recirculation bubble, the flow reattaches to the airfoil and remains attached right up to the TE. When comparing the different cases, the reduction of the mass flow rate delays the boundary layer transition and leads to larger turbulent structures in the separation region and in the downstream direction.

The flow topology around the rotor blades is then analyzed by means of the mean streamwise velocity component, u, (Figure 6) and the turbulent kinetic energy, k_t, (Figure 7), which have been averaged in the rotating reference frame. The averaged values are computed over 3.5 rotations of the fan. On the blade suction side, near the LE, a zone of negative velocity and high turbulent kinetic

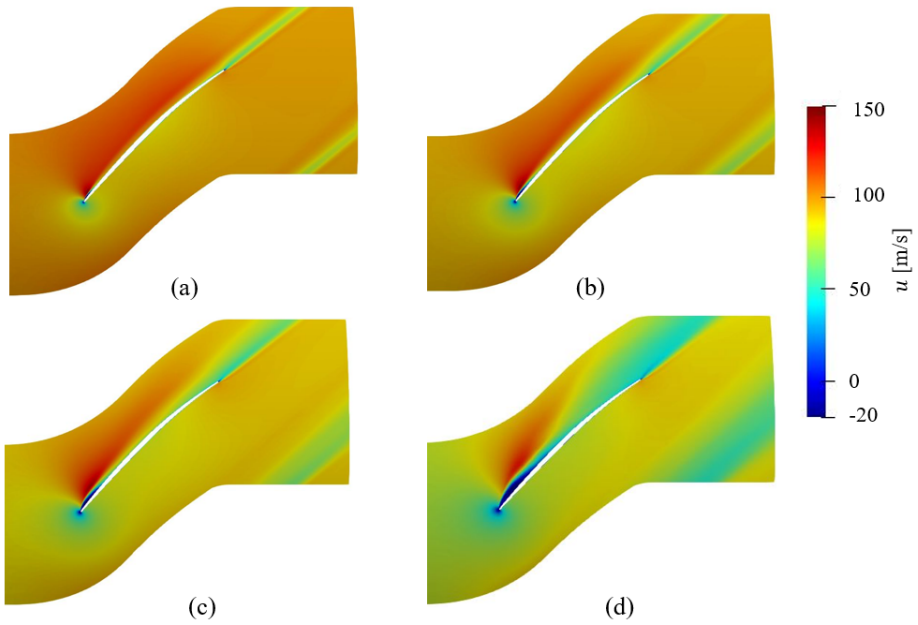

Figure 6: Contours of averaged streamwise velocity u around the rotor blade, for various mass flow rates, (a) $\dot{m} = 22$ kg/s, (b) $\dot{m} = 21$ kg/s, (c) $\dot{m} = 20$ kg/s and (d) $\dot{m} = 19$ kg/s.

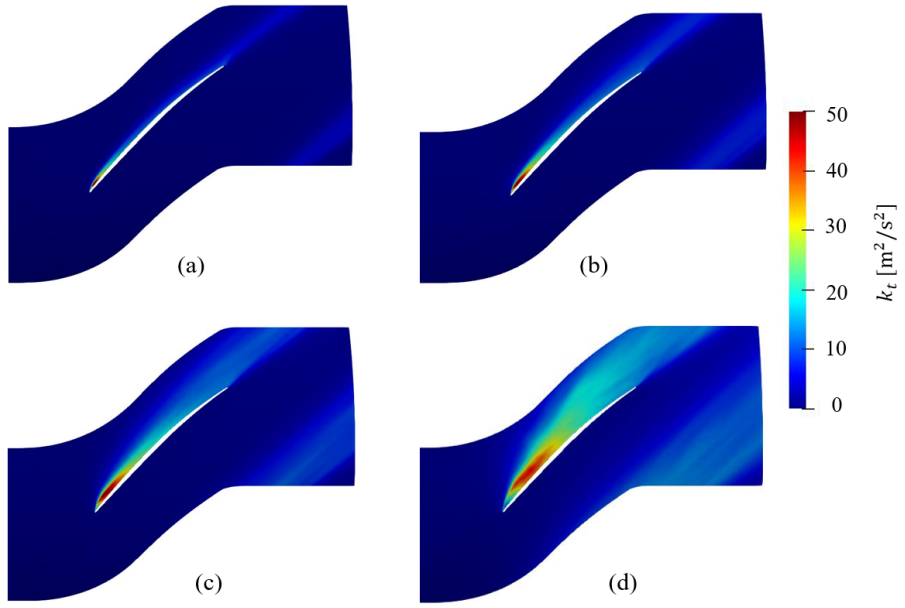

Figure 7: Contours of turbulent kinetic energy k_t around the rotor blade, for various mass flow rates, (a) $\dot{m} = 22$ kg/s, (b) $\dot{m} = 21$ kg/s, (c) $\dot{m} = 20$ kg/s and (d) $\dot{m} = 19$ kg/s.

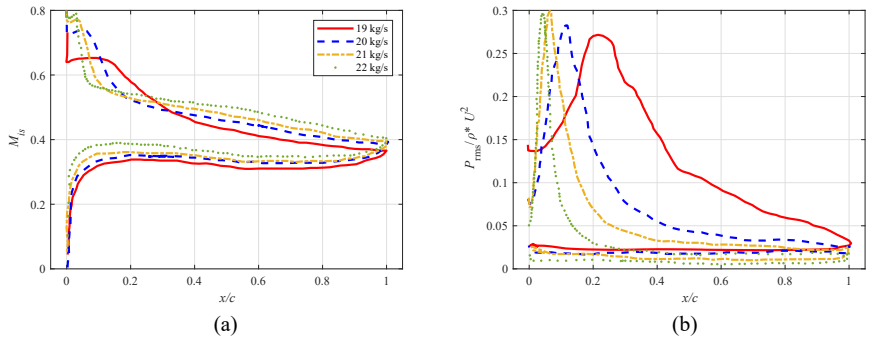

Figure 8: Average isentropic Mach number M_{is} (a) and RMS pressure fluctuations P_{rms} (b) along the rotor blade for various mass flow rates.

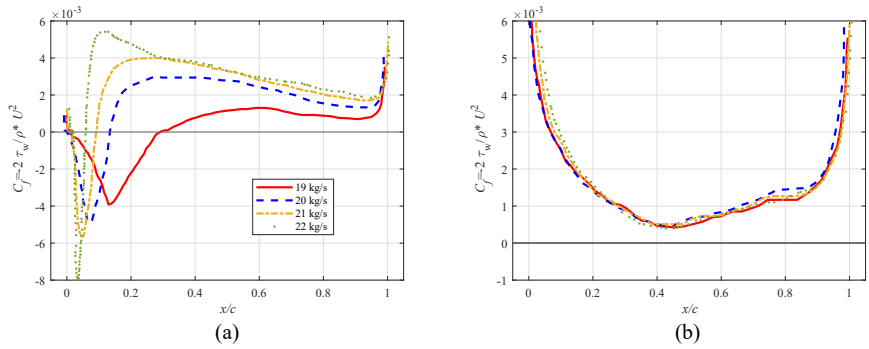

Figure 9: Average friction coefficient C_f along the rotor blade for various mass flow rates. (a) suction side. (b) pressure side.

energy can be found. This recirculation region corresponds to the bubble identified by the Q-criterion iso-surfaces in Figure 5, which leads to the boundary layer transition to turbulence. By comparing the flow topology obtained from the different cases, we can observe that as the mass flow rate decreases, the bubble position is shifted downstream over the suction side and the size of the bubble increases. However, smaller values of the maximum turbulent kinetic energy are observed when the mass flow rate decreases, which delays the transition to turbulence. Consequently, both the boundary layer thickness and the wake thickness increase when the mass flow rate is reduced.

The distribution of isentropic Mach number, M_{is}, which is related to the static pressure distribution on the blade, and the RMS of the pressure fluctuations (P_{rms}) along the blade are presented in Figure 8. For the different cases, the pressure side shows a favorable pressure gradient. On the suction side, a plateau of M_{is} can be observed near the LE, which indicate the presence of the recirculation bubble. Downstream of the bubble region, the turbulent boundary layer is subject to an adverse pressure gradient right up to the TE. The bubble

region also exhibits high P_{rms} values, as shown in Figure 8 (b). It can be observed that, as the mass flow rate decreases, the bubble is shifted downstream and its size increases, which is consistent with our previous findings from the flow topology. The strength of the additional self-noise source due to the recirculation bubble can be partly related to the P_{rms} levels. When the mass flow rate decreases, the maximum value of P_{rms} is lower, but the width of the peak increases. These changes are expected to have an impact on the noise radiated by this additional noise source.

The friction coefficient, C_f, can also provide useful information about the recirculation bubble. A comparison of C_f between the different mass flow rates is presented in Figure 9, over the suction side (a) and the pressure side (b) of the rotor blade. For all the cases, a region of negative friction coefficient is observed close to the LE of the blade on the suction side, which is related to the presence of the bubble. Downstream of this region, C_f remains positive along the suction side right up to the TE. The locations where C_f reaches zero can be considered as the initial and end points of the bubble, respectively, which allows us to define the size of the bubble. As for the analysis of M_{is} in Figure 8, the reattachment point is shifted downstream as the mass flow rate decreases, which leads to a larger recirculation bubble. On the pressure side, the distribution of C_f is quite similar for the different mass flow rates and remains positive, which suggests that the flow is attached all along the pressure side.

Several boundary layer parameters have been computed on the suction side of the rotor blade for the different mass flow rates and compared in Figure 10. The displacement thickness is defined as,

$$\delta_1 = \int_0^{\delta} (1 - \frac{\rho U}{\rho_0 U_0})\mathrm{dn}. \tag{2}$$

The momentum thickness is defined as,

$$\delta_2 = \int_0^{\delta} \frac{\rho U}{\rho_0 U_0}(1 - \frac{U}{U_0})\mathrm{dn}, \tag{3}$$

and the shape factor $H_{12} = \delta_1/\delta_2$, where n is the normal wall distance to the suction side surface of the blade, ρ_0 is the freestream density, and ρ and U are the density and the velocity magnitude in the boundary layer, respectively. The development of the boundary layer can be divided into three main regions, (i) the separation region, (ii) the reattachment region and (iii) the adverse pressure-gradient region. For all cases, near the LE, the displacement thickness δ_1 reaches a local maximum in the recirculation bubble, while the momentum thickness δ_2 is almost constant. Thus, in this region, large values of the shape factor H_{12} are reached. Downstream of the recirculation bubble, the boundary layer is reattached and the shape factor decreases significantly. As previously discussed, the streamwise location of the reattachment point varies significantly with the mass flow rate, from $0.1c$ for the highest mass flow rate ($\dot{m} = 22$ kg/s) to $0.35c$ for the smallest mass flow rate ($\dot{m} = 19$ kg/s). After the reattachment, a plateau is observed for the boundary layer parameters. The size of this plateau increases

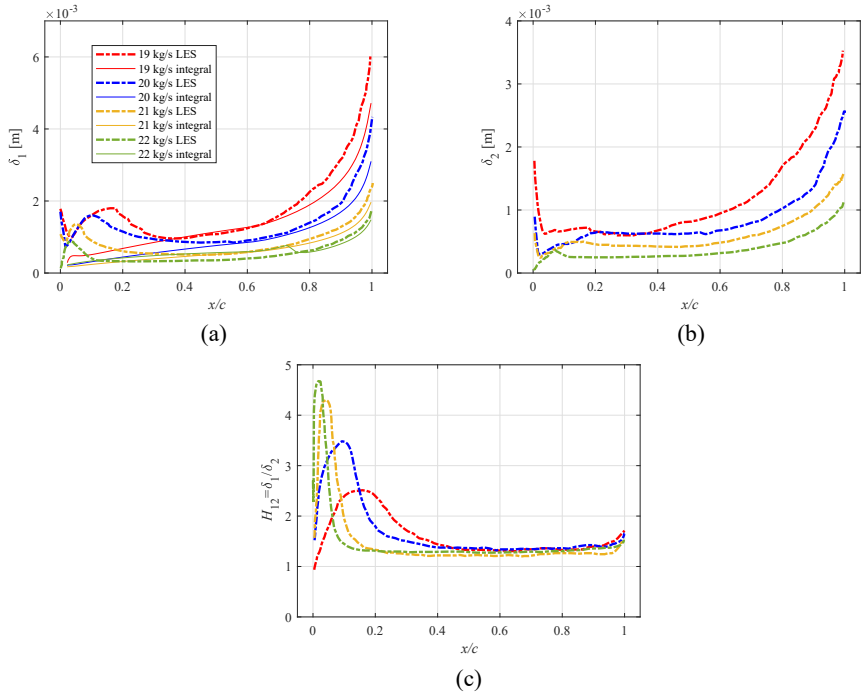

Figure 10: Comparison of boundary layer parameters on the suction side of the rotor blade for various mass flow rates. (a) Boundary layer displacement thickness δ_1, (b) momentum thickness δ_2, (c) and shape factor H_{12}.

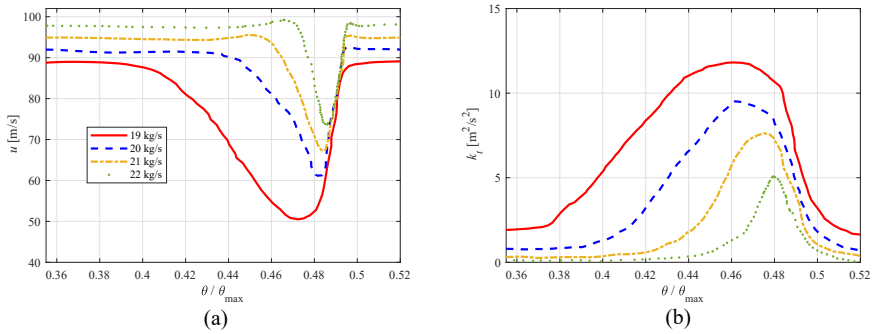

Figure 11: Comparison of the streamwise velocity component u (a) and k_t (b) profiles in the wake of the rotor blade, at one chord length from the TE.

with the mass flow rate. At further downstream locations, the combined effects of the adverse pressure gradient and the friction lead to an increase in both the displacement and momentum thicknesses while the shape factor remains nearly constant. By comparing the different cases, it can be observed that decreasing the mass flow rate leads to a thicker boundary layer with a larger separation region, and a reattachment point that is shifted further downstream.

The evolution of the boundary layer is controlled by several parameters, including the separation region due to the recirculation bubble, the pressure gradient and the skin friction. In order to study the effect of the recirculation bubble on the boundary layer, the displacement thickness has also been computed using the integral formulation available in the numerical software Xfoil [39, 40]. The results are compared to the LES computations for the different mass flow rates in Figure 10. When using the integral formulation in Xfoil, the boundary layer is assumed to be fully turbulent from the LE, such that there is no recirculation bubble. However, the levels of δ_1 obtained from the integral formulation have been adjusted to match the value of δ_1 in the LES at a given axial position by adding a constant value. This allows for the comparison of the δ_1 distribution, taking into account the effect of the bubble on the boundary layer thickness. The differences in the δ_1 distribution for the different mass flow rates are mainly due to differences in the angle of attack and Reynolds number. The results from the LES and the integral formulation for the different mass flow rates show similar trends once the boundary layer is reattached, whereas significant differences can be found in the separation and reattachment regions. This is particularly true for the large mass flow rates (21 kg/s and 22 kg/s), which suggests that downstream of the bubble, the boundary layer is fully turbulent and its thickness is only controlled by the pressure gradient and the skin friction. For small mass flow rates, discrepancies become significant due to the presence of a large recirculation bubble, which affects the boundary layer development over a larger region of the blade. Once the flow is reattached, the δ_1 distribution has a similar trend despite the differences in absolute value.

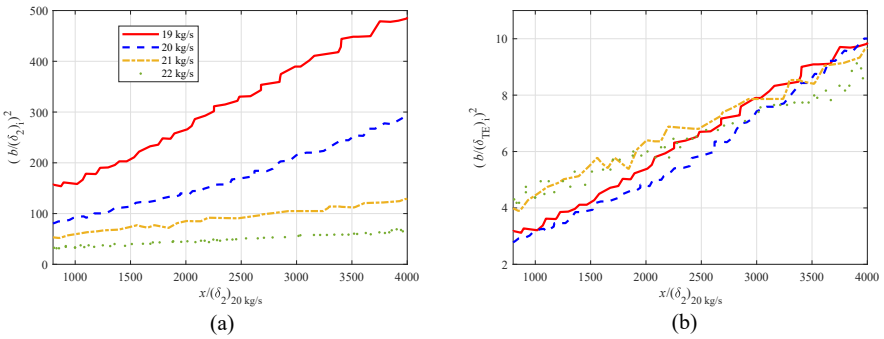

Figure 12: Streamwise evolution of the wake half-width b, normalized by the momentum thickness in the far wake δ_2 (a), and the boundary layer thickness at the blade TE δ_{TE} (b). x is the streamwise direction and $x = 0$ m corresponds to the blade TE.

Finally, the effect of the mass flow rate on the rotor wakes is studied. Figure 11 shows the distributions of streamwise velocity component u and the turbulent kinetic energy k_t at a distance of one chord length from the TE of the rotor blade. θ_{max} is the angular sector of a single fan blade passage, which corresponds to $2\pi/16$. When the mass flow rate decreases, the wake becomes thicker whereas both the velocity deficit and turbulent kinetic energy increase, which is consistent with results in Figures 6 and 7. For the largest mass flow rate case (22 kg/s), it seems that a symmetric Gaussian function could fit the circumferential distribution of k_t, whereas cases with a low mass flow rate show skewed wake profiles towards the suction side. The wake is further analyzed by calculating the wake half-width, b, which can be defined as the width of the wake where the velocity reaches 50% of the maximum velocity deficit. The axial evolution of the wake half-width is shown in Figure 12 (a), in which the variables have been normalized by the momentum thickness in the far-wake that is assumed to be constant for each case. It should be noted that the momentum thickness in the far-wake can be computed from Eq.3, which can be rewritten as $\delta_2 = \int_0^{\delta} \frac{\rho u}{\rho_0 U_0}(1 - \frac{u}{U_0})\mathrm{dn}$, where u corresponds to the streamwise component of the mean velocity in the wake, and U_0 corresponds to the freestream velocity magnitude outside the wake. Results in Figure 11 (a) are shown for the far-wake region ($x/\delta_2 > 800$), where the wake properties are assumed to have an asymptotic behavior and δ_2 is nearly constant. An apparent linear increase of b^2 with the downstream distance can be observed for the different cases. Furthermore, the wake half-width also increases as the mass flow rate decreases, which is consistent with the trends in the boundary layer thicknesses in Figure 10. Figure 12 (b) shows the evolution of b normalized by the boundary-layer thickness at the TE of the fan blade, δ_{TE}, that is defined as the wall-normal distance from the blade surface where the velocity reaches 99% of the freestream velocity. All cases seem to collapse onto a single trend, particularly beyond a streamwise distance where the wake is fully developed ($x/\delta_2 > 2500$). In this case, the evolution of

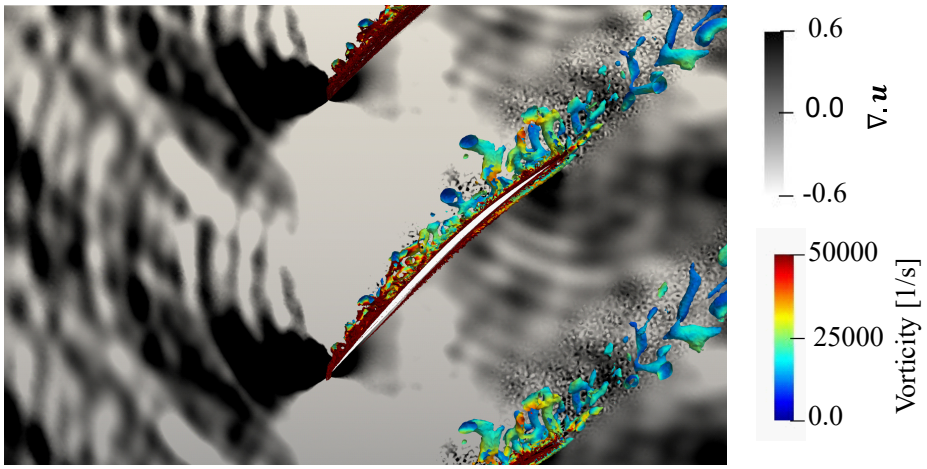

Figure 13: Instantaneous contours of dilatation rate and iso-surfaces of Q-criterion ($Qc^2/U_0^2 = 100$) colored by the vorticity magnitude at $\dot{m} = 20$ kg/s. The star symbol indicates the location of the monitor point where unsteady pressure samples were collected for the PSD computation. The dashed-line shows the location of the monitor points used for the calculation of the coherence.

the fan wake is controlled by the boundary layer thicknesses at the TE of the blade.

4.2. Aeroacoustic results

Contours of the instantaneous dilatation rate ($\nabla \cdot \mathbf{u}$) for $\dot{m} = 20\,\mathrm{kg/s}$ are shown in Figure 13, along with iso-surfaces of Q-criterion ($Qc^2/U_0^2 = 100$) colored by the vorticity magnitude. The development of turbulent structures around the blades and in the wakes can be observed. The contours of instantaneous dilatation rate show wave-fronts generated by the TE and the bubble region near the LE. The present simulations are able to capture the noise generation mechanisms at the TE and in the bubble region, as well as the acoustic wave propagation in the refined-mesh region around the fan stage. It should be noted that there are no acoustic reflections from the upstream and downstream boundaries of the domain. The turbulence in the fan wakes near the TE in Figure 13 does not seem to contribute to the radiated noise from the fan stage, which indicates that quadrupole noise sources from the wake are not dominant when compared to dipole noise sources from the blades.

The acoustic field is directly computed in the LES simulations up to one rotor chord length upstream of the rotor blades, in the mesh refinement region. A comparison of the PSD of the pressure fluctuations (p') for various mass flow rates is showed in Figure 14 (a). All PSD spectra are obtained by multiplying the pressure signals by a Hanning window with 50% overlap and by averaging the signals using 5 segments of length 2^{10}. A pressure reference of $P_{\mathrm{ref}} = 2.10^5$ Pa is adopted. The location of the monitor point used for the unsteady data collection is indicated by the star symbol in Figure 13. For the different cases, tones

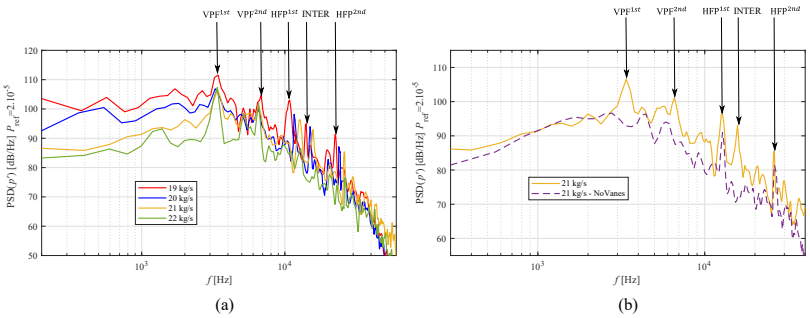

Figure 14: PSD of the pressure fluctuations from a monitor point in the normal direction to the rotor surface at one chord length from the rotor LE. (a) Rotor-stator simulations at various mass flow rates. (b) Comparison between rotor-stator and rotor-alone simulations at $\dot{m} = 21\,\mathrm{kg/s}$.

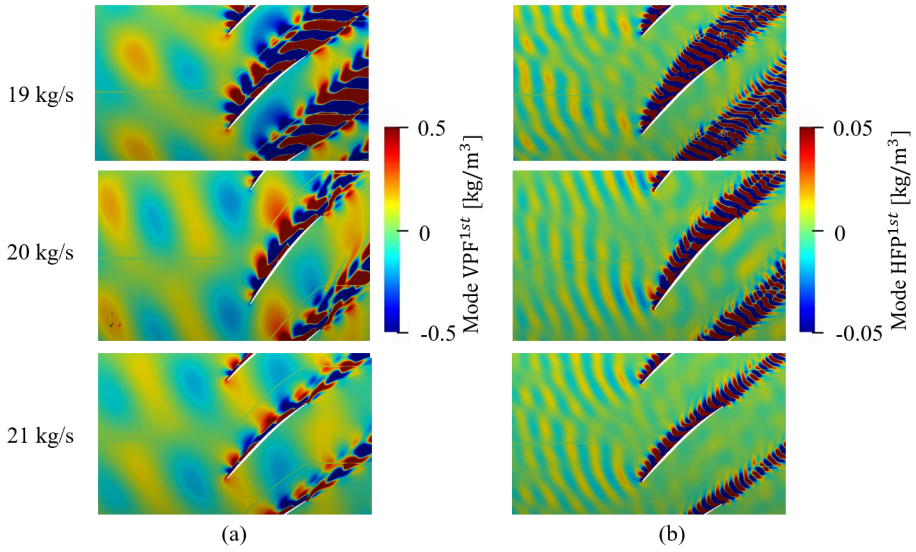

Figure 15: Spatial distribution of the density modes using the DMT technique. (a) VPF^{1st}. (b) HFP^{1st}.

at 3200 Hz and 6400 Hz can be observed. The frequencies at which these tones appear are independent of the mass flow rate and correspond to the first two harmonics of the Vane Passing Frequency VPF $= V\Omega/60$, where Ω is the rotation speed that is given in RPM, and $V = 32$ corresponds to the number of vanes in the full stage. The presence of tones at harmonics of the VPF for a monitor point that is rotating with the rotor domain can be associated with the noise emitted by the periodic interaction of the rotor blade wakes with the stator vanes. For a monitor point in the stator domain, this interaction is expected to generate noise at the BPF and its harmonics $\mathrm{BPF}_n = nB\omega$, where $\omega = \Omega/60$ and n corresponds to the order of the BPF harmonic. Using the Tyler and Sofrin rule [41], the acoustic modes that are generated by the interaction noise have azimuthal orders $m = nB - kV$, where k is an integer. If the monitor point is in a rotating reference frame, its angular position θ varies with time, such that $\theta(t) = \omega t$. Thus, for a duct mode of order m, the phase term of the pressure fluctuation that depends on θ and t in the rotating reference frame can be written as,

$$\mathrm{e}^{\mathrm{i}(m\theta(t)-\omega t)} = \mathrm{e}^{\mathrm{i}([nB-kV]\omega t - nB\omega t)} = \mathrm{e}^{-\mathrm{i}kV\omega t} \tag{4}$$

where i is the imaginary unit and the frequency $kV\omega$ corresponding to the VPF harmonics can be recognized.

At higher frequencies, between 10 kHz and 13 kHz, a peak is visible for each case, except for the largest mass flow rate ($\dot{m} = 22$ kg/s). This peak is referred to as HFP^{1st} in Figure 14. Its second harmonic, denoted HFP^{2nd}, can also be observed in Figure 14. When the mass flow rate increases, the frequency of these High Frequency Peaks (HFP) increases (e.g. from 10.5 kHz to 12.8 kHz for HFP^{1st}) whereas their amplitude decreases. For each case where HFP peaks are present, an additional peak denoted INTER in Figure 14 can be observed at a frequency $\mathrm{INTER} = \mathrm{HFP}^{1st} + \mathrm{VPF}^{1st}$. The HFP peaks are related to a noise mechanism associated with the recirculation bubble, and are discussed below, whereas the INTER peak is an interaction tone between HFP^{1st} and VPF^{1st}.
The effects of the stator on the generated noise can also be observed when comparing the acoustic spectra from the different mass flow rates in Figure 14 (a). As the mass flow rate is reduced, the turbulent kinetic energy in the boundary layers on the suction side of the rotor and in the rotor wakes is increased. Consequently, both the trailing edge noise and the rotor-stator interaction noise increase. In Figure 14 (a), it can be seen that the broadband noise component is increased with the reduction of the mass flow rate, which can be attributed to the increase in the size and turbulence intensity of the recirculation bubble. This can be partially explained by the rotor-stator interaction noise, which highlights the effect of the stator on the generated noise.
The broadband noise from the rotor-alone simulation can be compared to the rotor-stator interaction noise, which is considered to be the dominant noise source in a fan/OGV stage at approach conditions. The amplitude of the tones VPF^{1st} and HFP^{1st} are compared in Table 4 for various mass flow rates. For the different cases, the contribution of the rotor-stator interaction noise is shown to

Table 4: Comparison of the amplitude of the tones VPF^{1st} and HFP^{1st} for different mass flow rates.

$\dot{m}$ [kg/s]	$\|\mathrm{VPF}^{1st}\|$ [dB/Hz]	$\|\mathrm{HFP}^{1st}\|$ [dB/Hz]	$\Delta(\|\mathrm{VPF}^{1st}\|$ - $\|\mathrm{HFP}^{1st}\|)$ [dB/Hz]
19	111.0	103.5	7.5
20	107.0	98.6	8.4
21	106.2	96.6	9.6
22	106.0	86.5	19.5

be dominant. As the mass flow rate decreases, the amplitude of the tone at the VPF^{1st} increases. This is due to a more pronounced rotor wake deficit as the strength of the recirculation bubble increases (e.g. see Figure 6), which leads to an increase in the rotor-stator interaction noise. It is also useful to compare the amplitude of the HFP^{1st} from the lowest mass flow rate ($\dot{m} = 19$ kg/s) with the amplitude of the VPF^{1st} from the highest mass flow rate ($\dot{m} = 22$ kg/s), for which the bubble has limited influence on the rotor wakes. In this case, the difference between the HFP^{1st} ($\dot{m} = 19$ kg/s) and the VPF^{1st} ($\dot{m} = 22$ kg/s) is approximately 2.5 dB/Hz, which suggests that the tonal noise associated with the recirculation bubble can be of the same order of magnitude as the rotor-stator interaction noise in a stage without the presence of a recirculation bubble.

In order to better understand the effects of a recirculation bubble on the fan noise, an additional LES has been performed at $\dot{m} = 21$ kg/s without the stator vanes. Nevertheless, the stator domain without vanes that is downstream of the rotor is kept in the simulation in order to maintain the same length of the computational domain. The PSD of the pressure fluctuations obtained from the simulations at 21 kg/s, with and without the stator vanes, are compared in Figure 14 (b). As expected, the peaks at the VPFs and INTER frequencies are not present in the spectrum for the simulation without stator vanes. However, the HFPs can still be seen in the noise spectrum. The frequencies at which these tones appear are similar between the two cases, with and without the stator vanes, whereas their amplitudes are reduced in the case without stator vanes (a reduction of 5 dB/Hz for HFP^{1st} and 4 dB/Hz for HFP^{2nd}). Additionally, the absence of the stator vanes leads to a broadband noise reduction of 5 to 8 dB/Hz in the frequency range from 3 kHz up to the cut-off frequency (30 kHz). This shows that the rotor-stator interaction noise, which is due to the interaction of the rotor wakes with the stator vanes, is a significant noise source that is increased by the presence of a recirculation bubble.

The tones observed in Figure 14 can be further investigated using a mode decomposition technique, which is known as Dynamic Mode Tracking (DMT) [42]. The DMT has been developed to study the spatial and temporal features of the flow at a given frequency. It has the advantage to be an "on-the-fly" method, which is useful to reduce the computational expense and data storage requirements. Figure 15 shows DMT results calculated from the density in the LES

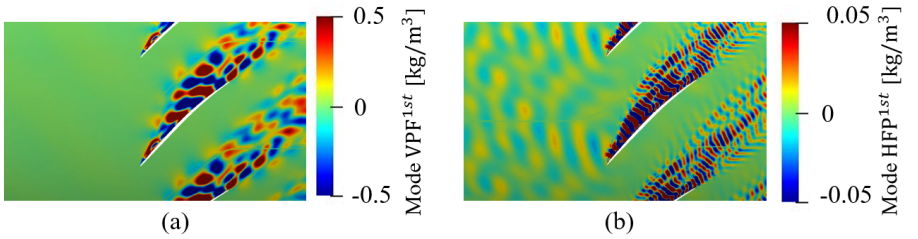

Figure 16: Spatial distribution of the density modes using the DMT technique for the case at $\dot{m} = 21$ kg/s without stator vanes. (a) VPF^{1st}. (b) HFP^{1st}.

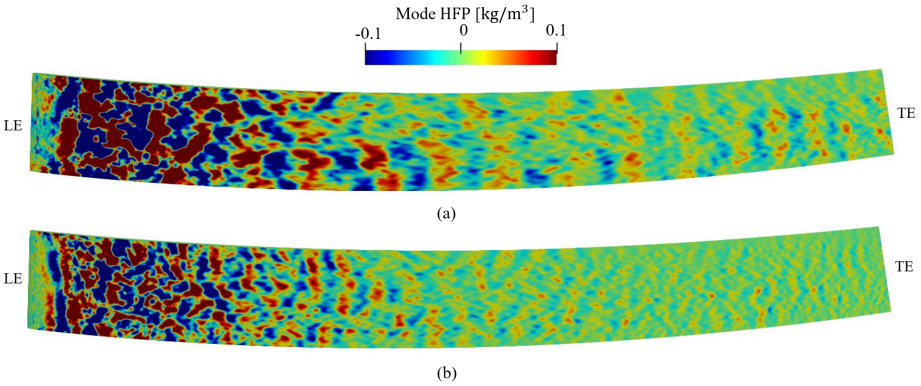

Figure 17: Spatial distribution of the density modes using the DMT technique on the suction side of the rotor blade at $\dot{m} = 19$ kg/s. (a) HFP^{1st}. (b) HFP^{2nd}.

with the stator vanes at VPF^{1st} and HFP^{1st}, for various mass flow rates. Figure 16 shows the DMT results for the simulation without the stator vanes, at $\dot{m} = 21$ kg/s. For the simulations with stator vanes, the mode that is related to the VPF^{1st} shows wave-like fluctuations coming from downstream of the rotor and propagating in the upstream direction (An animated sequence is provided as supplementary material (movie 1)), through the blade passage. For the simulation without the stator vanes, the upstream propagating density fluctuations are not observed in Figure 16(a). Thus, the behavior of this mode at the VPF^{1st} confirms that the peaks observed at this frequency in Figure 14 are associated with the interaction tones between the periodic rotor wakes and the stator vanes.

The DMT results computed at the HFP^{1st} in Figures 15 and 16 show a density mode in the boundary layer that is convected by the flow, and another mode generated in the bubble region that propagates in the upstream direction (An animated sequence is provided as supplementary material (movie 2)). The latter can be associated with acoustic waves and confirms that the peak observed at the HFP^{1st} in Figure 14 is generated by a noise source located in the bubble region.

In Figure 17, the spatial distribution of the density modes from the DMT

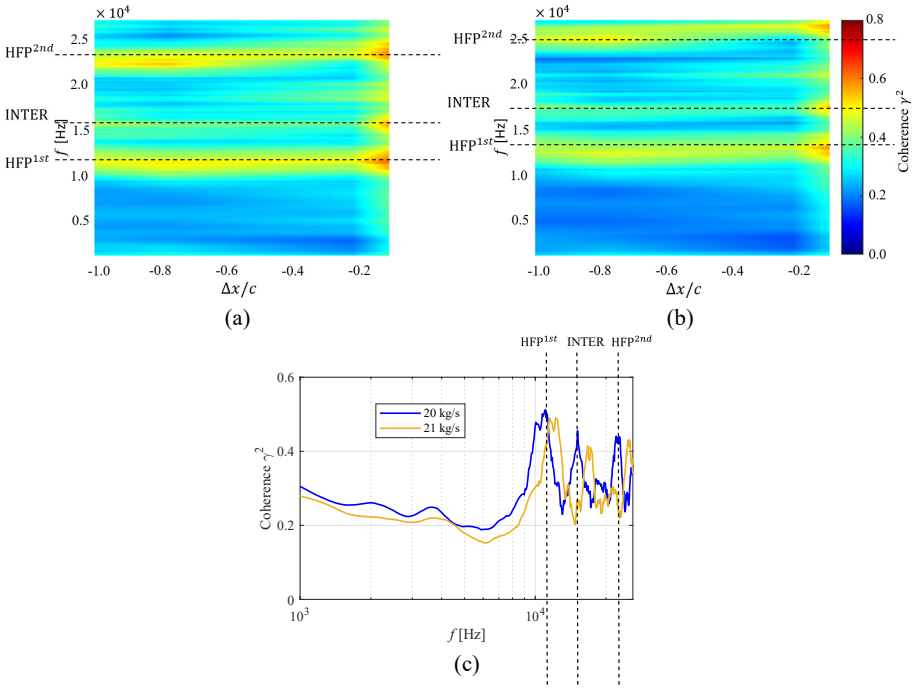

Figure 18: Coherence between the pressure fluctuations in the bubble region and the pressure fluctuations upstream of the rotor blade and normal to the LE. (a) $\dot{m} = 20$ kg/s and (b) $\dot{m} = 21$ kg/s. (c) Coherence at $\Delta x/c = -1$. The origin of the x axis is the rotor LE.

technique at HFP^{1st} and HFP^{2nd} is shown on the suction side of the rotor blade for a mass flow rate $\dot{m} = 19$ kg/s. The maximum value can be found in the separation region close to the LE and the modes travel towards the TE. Thus, the TE noise is expected to be affected by disturbances that are generated by the recirculation bubble.

In order to better understand the noise sources, the coherence between pressure fluctuations in the separation region of the rotor blade and pressure fluctuations at several positions upstream of the rotor is calculated for $\dot{m} = 20$ kg/s and $\dot{m} = 21$ kg/s. The location of 100 monitor points is shown by a dashed line in Figure 13. The coherence between the both signals is defined as,

$$\gamma^2_{p_w p'}(f) = \frac{|S_{p_w p'}(f)|^2}{S_{p_w p_w}(f) S_{p'p'}(f)}, \tag{5}$$

where $S_{p_w p_w}$ is the spectral density of the wall pressure fluctuations p_w in the separation region, $S_{p'p'}$ is the spectral density of the pressure fluctuations p' at a probe location upstream of the rotor blade, and $S_{p_w p'}$ is the cross-spectral density between p_w and p'. The resulting coherences are presented in Figure 18 (a) and (b) as a function of the frequency and the distance $\Delta x/c$ between the reference point on the blade surface and the monitor point located in the

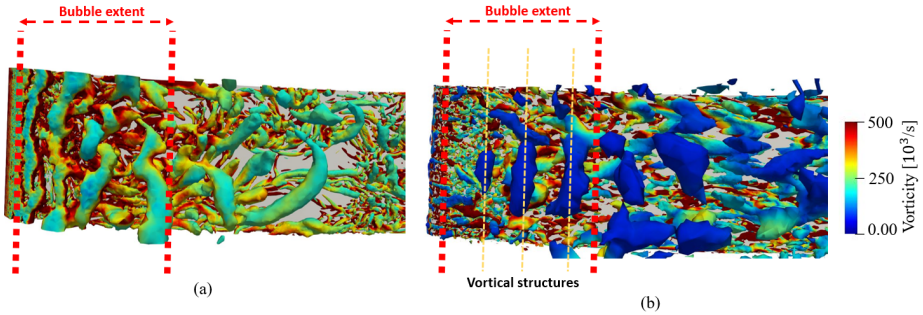

Figure 19: Iso-surfaces of Q-criterion ($Qc^2/U_0^2 = 5000$), colored by the vorticity magnitude, for the mass flow rate $\dot{m} = 20$ kg/s. (a) Instantaneous flow field. (b) Mode using the DMT technique at HFP^{1st}.

Table 5: Strouhal number St parameters for various mass flow rates. $\delta_{1,\text{bubble}}$ corresponds to the local maximum of the boundary layer displacement thickness δ_1 in the separation region.

$\dot{m}$ [kg/s]	U_0 [m/s]	$\delta_{1,\text{bubble}}$ [mm]	HFP^{1st} frequency [kHz]	St
19	80	1.81	10.5	0.237
20	84	1.61	11.6	0.222
21	88	1.38	12.8	0.201

upstream direction. Additionally, the coherence spectrum farthest to the blade surface (at $\Delta x/c = -1$) is plotted in Figure 18 (c) for $\dot{m} = 20$ kg/s and $\dot{m} = 21$ kg/s. All cases show high coherence levels and large peaks in the spectra at the high frequency peaks HFP^{1st}, HFP^{2nd} and INTER up to a large distance away from the recirculation bubble.

Results from the coherence analysis confirm the observations made using the DMT technique (Figures 15 and 17). Thus, the bubble region can be considered as an additional source of fan noise that produce high frequency peaks in the noise spectra. The low coherence in Figure 18 at the VPF^{1st} and VPF^{2nd} also confirms that the bubble region does not contribute to the peaks observed in the acoustic spectra at these frequencies. In Figure 18 (c), the frequencies of the peaks HFP^{1st}, HFP^{2nd} and INTER are increasing with the mass flow rate, which can be related to the reduced size of the bubble and it is consistent with the results in the acoustic spectra in Figure 14. The coherence of the peaks are slightly higher for the lowest mass flow rate. Since the noise produced by the bubble region at the HFPs is higher for the reduced mass flow rates, a significant contribution to the overall noise level at these frequencies might be attributed to the bubble region, which leads to high coherence levels in Figure 18.

The physical mechanism which cause the HFPs in the acoustic spectra is also investigated. To this end, a snapshot of the turbulent structures is shown in Figure 19 (a) (An animated sequence is provided as supplementary material (movie 3)) near the LE of the blade for the mass flow rate $\dot{m} = 20$ kg/s.

Note that similar turbulent structures were obtained for other mass flow rates. The laminar boundary layer close to the leading edge detaches in the presence of a strong pressure gradient, and nearly bi-dimensional vortices are formed. Then, the vortical structures are subject to strong spanwise deformations as they are convected in the downstream direction. In order to investigate the relation between these vortical structures and the noise at the HFPs, Figure 19 (b) shows iso-surfaces of Q-criterion based on the filtered flow field from the DMT at HFP^{1st}. Turbulent structures at this frequency can thus be identified. 2D structures are formed once again in the bubble region and convected in the downstream direction. This indicates that the HFP^{1st} in the acoustic spectra is related to a mechanism of vortex shedding in the bubble region. A Strouhal number, defined as $St = f_v L/U_0$, where f_v is the frequency of the vortex shedding, L is a length scale and U_0 is the free-stream velocity magnitude upstream of the fan, is calculated for each case. For a vortex shedding mechanism, the length scale is usually chosen as a characteristic length in the direction normal to the incoming flow. Here, we propose to use the local maximum of the boundary layer displacement thickness δ_1 in the separation region, as shown in Figure 10 (a). For a vortex shedding at the HFP^{1st}, the Strouhal numbers calculated for each case are shown in Table 5. The values of Strouhal number obtained are typical of a vortex shedding mechanism ($St \approx 0.2$). This confirms that the noise radiated from the bubble region at the HFP^{1st} is associated with a vortex shedding mechanism.

5. Conclusion

A set of wall-resolved LES has been performed over a radial slice of a scale model UHBR fan stage at approach conditions, for different values of the mass flow rate. In order to reduce the computational cost, a periodic sector with a single blade and two OGVs has been considered. The meshes have been designed to ensure that the acoustic waves can be propagated to all monitor points in the frequency range of interest.

For the different mass flow rates, a laminar separation bubble is observed on the suction side near the blade leading edge, which causes the boundary layer transition to turbulence. The size and position of the recirculation bubble, as well as the amplitude of the pressure disturbances in the separation region, appear to vary significantly with the mass flow rate. As the mass flow rate decreases, the size of the bubble increases, the bubble shifts towards donwstream locations, and high levels of wall pressure fluctuations can be found along the suction side of the blade. The development of the boundary layer and the wake is influenced by the presence of a recirculation bubble and its size. For a low mass flow rate and a large recirculation bubble, both the boundary layer thickness on the suction side and the wake width increase. However, the boundary layer on the pressure side appears to be unchanged for all mass flow rates. It has been found that the evolution of the wake width far downstream of the fan blade scales with the boundary layer thickness at the trailing edge.

Two different self-noise mechanisms have been identified on the rotor blade: the trailing-edge noise generated by the scattering of the turbulent boundary layer at the trailing edge, and an additional noise source due to the recirculation bubble near the leading edge. High frequency peaks in the noise spectra are associated with the recirculation bubble. This noise generation mechanism has been studied in detail by using a DMT technique. It has been found that the acoustic waves that are related to the first harmonic of the high frequency peak come from the bubble region. This finding is consistent with the results of the coherence between the wall pressure fluctuations in the recirculation bubble region and pressure fluctuations away from the blade.

The frequency of the tones from the bubble decreases with the mass flow rate, and the amplitude of the tones increases. An interaction tone between the recirculation bubble and the stator vanes has been found by analyzing an additional simulation performed without the stator vanes. Additionally, the broadband noise levels have been found to increase for the low mass flow rates over the whole frequency range.

Finally, iso-surfaces of Q-criterion have been computed using the DMT technique at the first high frequency peak to investigate the physical mechanism of the noise from the recirculation bubble. This analysis suggests that a vortex shedding from the bubble explains the noise radiated at this frequency.

It has been shown that the noise radiated from a recirculation bubble can be a significant contributor to the fan noise. This noise source can be found at approach conditions, as the mass flow rate of an aero-engine is reduced. Thus, it might be useful to identify the presence of a recirculation bubble on fan blades using high-fidelity models to reduce this noise source at an early design stage.

Acknowledgments

This work was performed within the framework of the industrial chair ARENA (ANR-18-CHIN-0004-01) co-financed by Safran Aircraft Engines and the French National Research Agency (ANR), and is also supported by the Labex CeLyA of the Université de Lyon, operated by the French National Research Agency (ANR-11-LABX-0060/ ANR-16-IDEX-0005).
The computational resources were provided by GENCI (CINES, projects numbers A0082A05039 and A0102A05039) and by FLMSN-PMCS2I at Ecole Centrale de Lyon.

References

[1] E. Envia, Fan noise reduction: an overview, International Journal of Aeroacoustics 1 (1) (2002) 43–64. doi:10.1260/1475472021502668.

[2] S. Moreau, Turbomachinery noise predictions: Present and future, Acoustics 1 (1) (2019) 92–116. doi:10.3390/acoustics1010008.

[3] G.J.J. Ruijgrok, Elements of Aviation Acoustics, Delft University Press, 2004.

[4] N. Peake, A. B. Parry, Modern challenges facing turbomachinery aeroacoustics, Annual Review of Fluid Mechanics 44 (2012) 227–248. doi:10.1146/annurev-fluid-120710-101231.

[5] S. Oerlemans, P. Sijtsma, B. Méndez López, Location and quantification of noise sources on a wind turbine, Journal of Sound and Vibration 299 (4-5) (2007) 869–883. doi:https://doi.org/10.1016/j.jsv.2006.07.032.

[6] S. Bianchi, A. Corsini, A. Sheard, A critical review of passive noise control techniques in industrial fans, Journal of engineering for gas turbines and power 136 (4) (2014) 044001. doi:https://doi.org/10.1115/1.4025837.

[7] L. Leylekian, M. Lebrun, P. Lempereur, An overview of aircraft noise reduction technologies., Aerospace Lab (6) (2014) p. 1–15. doi:10.12762/2014.AL07-01.

[8] R. K. Amiet, Acoustic radiation from an airfoil in a turbulent stream, Journal of Sound and Vibration 41 (4) (1975) 407–420. doi:https://doi.org/10.1016/S0022-460X(75)80105-2.

[9] M. Roger, S. Moreau, Back-scattering correction and further extensions of Amiet's trailing-edge noise model. Part 1: theory, Journal of Sound and Vibration 286 (3) (2005) 477–506. doi:https://doi.org/10.1016/j.jsv.2004.10.054.

[10] C. Pérez Arroyo, T. Leonard, M. Sanjosé, S. Moreau, F. Duchaine, Large eddy simulation of a scale-model turbofan for fan noise source diagnostic, Journal of Sound and Vibration 445 (2019) 64–76. doi:https://doi.org/10.1016/j.jsv.2019.01.005.

[11] S.-x. Shi, Y.-z. Liu, J.-m. Chen, An experimental study of flow around a bio-inspired airfoil at Reynolds number 2.0×10^3, Journal of Hydrodynamics 24 (3) (2012) 410–419. doi:https://doi.org/10.1016/S1001-6058(11)60262-X.

[12] H. Hu, Z. Yang, An Experimental Study of the Laminar Flow Separation on a Low-Reynolds-Number Airfoil, Journal of Fluids Engineering 130 (5). doi:https://doi.org/10.1115/1.2907416.

[13] T. Michelis, S. Yarusevych, M. Kotsonis, On the origin of spanwise vortex deformations in laminar separation bubbles, Journal of Fluid Mechanics 841 (2018) 81–108. doi:10.1017/jfm.2018.91.

[14] J. W. Kurelek, M. Kotsonis, S. Yarusevych, Transition in a separation bubble under tonal and broadband acoustic excitation, Journal of Fluid Mechanics 853 (2018) 1–36. doi:10.1017/jfm.2018.546.

[15] R.D. Sandberg, N. D. Sandham, Direct numerical simulation of turbulent flow past a trailing edge and the associated noise generation, Journal of Fluid Mechanics 596 (2008) 353–385. doi:10.1017/S0022112007009561.

[16] R.D. Sandberg, L. Jones, N. Sandham, P. Joseph, Direct numerical simulations of tonal noise generated by laminar flow past airfoils, Journal of Sound and Vibration 320 (4) (2009) 838–858. doi:https://doi.org/10.1016/j.jsv.2008.09.003.

[17] L. E. Jones, N. D. Sandham, R. D. Sandberg, Acoustic source identification for transitional airfoil flows using cross correlations, AIAA Journal 48 (10) (2010) 2299–2312. doi:https://doi.org/10.2514/1.J050345.

[18] H. Wu, M. Sanjosé, S. Moreau, R. D. Sandberg, Direct numerical simulation of the self-noise radiated by the installed controlled-diffusion airfoil at transitional Reynolds number, in: 2018 AIAA/CEAS Aeroacoustics Conference, 2018. doi:https://doi.org/10.2514/6.2018-3797.

[19] M. Deuse, R. D. Sandberg, Different noise generation mechanisms of a controlled diffusion aerofoil and their dependence on Mach number, Journal of Sound and Vibration 476. doi:https://doi.org/10.1016/j.jsv.2020.115317.

[20] S. Shubham, R. D. Sandberg, S. Moreau, H. Wu, Surface pressure spectrum variation with Mach number on a CD airfoil, Journal of Sound and Vibration 526. doi:https://doi.org/10.1016/j.jsv.2022.116762.

[21] C. Ho, P. Huerre, Perturbed free shear layers, Annual Review of Fluid Mechanics 16 (1) (1984) 365–422. doi:10.1146/annurev.fl.16.010184.002053.

[22] J. H. Watmuff, Evolution of a wave packet into vortex loops in a laminar separation bubble, Journal of Fluid Mechanics 397 (1999) 119–169. doi:10.1017/S0022112099006138.

[23] S. S. Diwan, O. N. Ramesh, On the origin of the inflectional instability of a laminar separation bubble, Journal of Fluid Mechanics 629 (2009) 263–298. doi:10.1017/S002211200900634X.

[24] S. Moreau, M. Sanjosé, F. Perot, M.-S.kim, Direct self-noise simulation of the installed controlled diffusion airfoil, 17th AIAA/CEAS Aeroacoustics Conference (32nd AIAA Aeroacoustics Conference) (2011) 2716.doi:https://doi.org/10.2514/6.2011-2716.

[25] D. Lewis, S. Moreau, M. C. Jacob, On the use of RANS-informed analytical models to perform broadband rotor-stator interaction noise predictions, in: 25th AIAA/CEAS Aeroacoustics Conference, 2019. doi:https://doi.org/10.2514/6.2019-2667.

[26] D. Lewis, S. Moreau, M. C. Jacob, M. Sanjosé, ACAT1 fan stage broadband noise prediction using large-eddy simulation and analytical models, AIAA Journal 60 (1) (2022) 360–380. doi:https://doi.org/10.2514/1.J060163.

[27] D. Casalino, A. Hazir, A. Mann, Turbofan broadband noise prediction using the lattice Boltzmann method, AIAA Journal 56 (2) (2018) 609–628. doi:https://doi.org/10.2514/1.J055674.

[28] A. Shabbir, C. R. Berndt, A. Breeze-Stringfellow, Turbomachine airfoil to reduce laminar separation, US Patent, Pub. No.: US 2021/0156258 A1 (2021).

[29] C. Brandstetter, V. Pagès, P. Duquesne, X. Ottavy, P. Ferrand, S. Aubert, L. Blanc, UHBR open-test-case fan ECL5/CATANA part 1: Geometry and aerodynamic performance, in: 14th European Conference on Turbomachinery Fluid dynamics & Thermodynamics, Gdansk, Poland, 2021.

[30] V. Pagès, P. Duquesne, X. Ottavy, P. Ferrand, S. Aubert, L. Blanc, C. Brandstetter, UHBR open-test-case fan ECL5/CATANA, part 2: Mechanical and aeroelastic stability analysis, in: 14th European Conference on Turbomachinery Fluid dynamics & Thermodynamics, Gdansk, Poland, 2021.

[31] M. M. Rai, N. K. Madavan, Multi-Airfoil Navier–Stokes Simulations of Turbine Rotor–Stator Interaction, Journal of Turbomachinery 112 (3) (1990) 377–384. doi:10.1115/1.2927670.

[32] T. Schonfeld, M. Rudgyard, Steady and unsteady flow simulations using the hybrid flow solver AVBP, AIAA Journal 37 (11) (1999) 1378–1385. doi:https://doi.org/10.2514/2.636.

[33] G. Wang, F. Duchaine, D. Papadogiannis, I. Duran, S. Moreau, L. Y. Gicquel, An overset grid method for large eddy simulation of turbomachinery stages, Journal of Computational Physics 274 (2014) 333–355. doi:https://doi.org/10.1016/j.jcp.2014.06.006.

[34] O. Colin, M. Rudgyard, Development of high-order Taylor-Galerkin schemes for LES, Journal of Computational Physics 162 (2) (2000) 338–371. doi:https://doi.org/10.1006/jcph.2000.6538.

[35] F. Nicoud, H. B. Toda, O. Cabrit, S. Bose, J. Lee, Using singular values to build a subgrid-scale model for large eddy simulations, Physics of fluids 23 (8). doi:https://doi.org/10.1063/1.3623274.

[36] T. Poinsot, S. Lele, Boundary conditions for direct simulations of compressible viscous flows, Journal of Computational Physics 101 (1) (1992) 104–129. doi:https://doi.org/10.1016/0021-9991(92)90046-2.

[37] J. Al-Am, V. Clair, A. Giauque, J. Boudet, F. Gea-Aguilera, A parametric study on the LES numerical setup to investigate fan/OGV broadband noise, International Journal of Turbomachinery, Propulsion and Power 6 (2). doi:10.3390/ijtpp6020012.

[38] J. Boudet, J.-F. Monier, F. Gao, Implementation of a roughness element to trip transition in large-eddy simulation, Journal of Thermal Science 24 (1) (2015) 30–36. doi:10.1007/s11630-015-0752-8.

[39] M. Drela, M. B. Giles, Viscous-inviscid analysis of transonic and low Reynolds number airfoils, AIAA Journal 25 (10) (1987) 1347–1355. doi:https://doi.org/10.2514/3.9789.

[40] M. Drela, Xfoil: An analysis and design system for low Reynolds number airfoils, in: Low Reynolds number aerodynamics, Springer, 1989, pp. 1–12. doi:10.1007/978-3-642-84010-4_1.

[41] J. Tyler, T. Sofrin, Axial flow compressor noise studies, Society of Automotive Engineers Transactions 70 (1962) 309–332. doi:https://doi.org/10.4271/620532.

[42] M. Queguineur, L. Gicquel, F. Dupuy, A. Misdariis, G. Staffelbach, Dynamic mode tracking and control with a relaxation method, Physics of Fluids 31 (3). doi:https://doi.org/10.1063/1.5085474.